

End-to-End Framework for Predicting the Remaining Useful Life of Lithium-Ion Batteries

Khoa Tran^{a,1}, Tri Le^{a,1}, Bao Huynh^{a,1}, Hung-Cuong Trinh^{b,*},
Vy-Rin Nguyen^c

^a*AIWARE Limited Company, 17 Huynh Man Dat Street, Hoa Cuong Bac Ward, Hai Chau District, Da Nang, 550000, Vietnam*

^b*Faculty of Information Technology, Ton Duc Thang University, Ho Chi Minh City, 700000, Vietnam*

^c*Software Engineering Department, FPT University, Da Nang, 550000, Vietnam*

Abstract

Accurate prediction of the Remaining Useful Life (RUL) is essential for enabling timely maintenance of lithium-ion batteries, impacting the operational efficiency of electric applications that rely on them. This paper proposes a RUL prediction approach that leverages data from recent charge-discharge cycles to estimate the number of remaining usable cycles. The approach introduces both a novel signal processing pipeline and a deep learning prediction model. In the signal preprocessing pipeline, a derived capacity feature $\dot{Q}(I, Q)$ is computed based on current and capacity signals. Alongside original capacity, voltage and current, these features are denoised and enhanced using statistical metrics and a delta-based method to capture differences between the current and previous cycles. In the prediction model, the processed features are then fed into a hybrid deep learning architecture composed of 1D Convolutional Neural Networks (CNN), Attentional Long Short-Term Memory (A-LSTM), and Ordinary Differential Equation-based LSTM (ODE-LSTM) modules. This architecture is designed to capture both local signal characteristics and long-range temporal dependencies while modeling the continuous-time dynamics of battery degradation. The model is further evaluated using transfer learning across different learning strategies and target data partitioning scenarios. Results indicate that the model maintains

*Corresponding author: trinhhungcuong@tdtu.edu.vn

¹These authors contributed equally to this work.

robust performance, even when fine-tuned on limited target data. Experimental results on two publicly available large-scale datasets demonstrate that the proposed method outperforms a baseline deep learning approach and machine learning techniques, achieving an RMSE of 101.59, highlighting its strong potential for real-world RUL prediction applications.

Keywords—Battery Health Management, Lithium-ion Batteries, Remaining Useful Life, Signal Processing, Deep Learning

1. Introduction

The growing global emphasis on sustainable energy has accelerated the advancement of battery technologies in recent years. Consequently, the lithium-ion battery (LIB) market is projected to surpass 170 billion USD by 2030 [26]. LIBs are widely used in applications such as grid energy storage systems, electric vehicles (EVs), and drones, all of which increasingly depend on effective Battery Health Management (BHM) systems [37, 5, 12] to ensure reliable performance. Typical BHM systems include key functionalities such as state of charge (SOC) estimation [28, 35], state of health (SOH) estimation [38, 20, 7], and remaining useful life (RUL) prediction [24, 23]. Among these, RUL prediction—which estimates the number of charge-discharge cycles remaining before a battery reaches its end-of-life (EOL)—is particularly crucial due to its implications for proactive maintenance, and safety assurance. During operation, LIBs undergo multiple forms of degradation during cycling, primarily caused by the loss of lithium inventory (LLI) and loss of active material (LAM) [25]. These challenges underscore the need for accurate RUL prediction models, not only to support real-time diagnostics and timely maintenance, but also to inform battery design [11].

In modern RUL prediction for LIBs, methods are mainly classified into two categories: curve-based and cycle-feature-based approaches. Curve-based methods model the degradation of a health indicator (e.g., capacity) over cycles using predefined functions (e.g., exponential decay), such as the double exponential model (DEM) [21], variational mode decomposition (VMD) [9], or empirical mode decomposition (EMD) [18, 15]. By fitting the historical data, these methods extrapolate the cycle at which the indicator falls below a predefined EOL threshold (e.g., 80% capacity [34]), thereby yielding the predicted number of remaining charge-discharge cycles (RUL). However, these methods have limited flexibility, as they assume a

fixed degradation trend throughout the entire battery cycle life, which may not accurately capture real-world variability. Moreover, they often require a long degradation history to make accurate predictions. For instance, the method in [41] relies on data from the first 450 charge-discharge cycles to perform accurate RUL prediction, making it unsuitable for early-stage prognostics. In contrast, cycle-feature-based methods extract meaningful features from a few recent cycles [45, 22], enabling more adaptive, earlier predictions under different operating conditions across charge-discharge cycles.

In recent cycle-feature-based approaches, [45] predicts RUL of LIBs using only features extracted from the current charge-discharge cycle. The features including discharge capacity, initial battery capacity, and working condition-derived variables. However, this approach neglects the short-term degradation trends observable in the preceding cycles, which are critical for accurately capturing the battery’s dynamic aging behavior. Although [45] reports promising results, these outcomes are partially influenced by an imbalanced data split—70 batteries for training and only 7 for testing—which may lead to overfitting and reduced generalizability. In another study, [49] employs features extracted from the incremental capacity (IC) curve of a partial segment of the current charge-discharge cycle to predict the SOH and RUL. However, the method is evaluated only on a small battery dataset comprising just four battery cells discharged under constant current. This results in highly similar data distributions between the training and testing sets, making the prediction task easier and less representative of real-world scenarios. In contrast, a more robust and realistic approach is presented in [22], where features are extracted from 10 selected cycles within the 30 most recent charge-discharge cycles to predict RUL. This strategy effectively captures recent degradation patterns, enhancing predictive performance. Furthermore, [22] incorporates transfer learning to leverage degradation knowledge from a different source domain, improving the prediction accuracy in the target domain. Their method is validated on one of the largest publicly available battery datasets, comprising 55 cells for training and 22 cells for testing, with diverse discharge profiles to simulate real-world conditions.

In this work, we adopt the standard approach introduced in [22], where a window of sequential charge-discharge cycles is used as input to predict the number of remaining operational cycles. Our proposed method features a novel signal preprocessing pipeline and a hybrid deep learning (DL) prediction model. The signal preprocessing incorporates a newly derived feature based on interpolation; the gathered features then undergo denoising, fea-

ture extraction, and delta computation. The DL architecture comprises two parallel branches: a 1D Convolutional Neural Network (CNN) block for spatial feature extraction, and a recurrent branch that employs an Attentional Long Short-Term Memory (A-LSTM) network [16] to capture temporal dependencies, along with a Long Short-Term Memory Ordinary Differential Equation (LSTM-ODE) block to enhance dynamic sequence modeling capabilities. Both the CNN and LSTM-ODE blocks are custom-designed. We also evaluate the proposed hybrid DL model using transfer learning under various learning strategies and source data splitting scenarios. The results demonstrate that our model remains robust even when trained on limited source data. The model is validated on two of the most widely used lithium-ion battery datasets: one with varying charging profiles [34] and the other with diverse discharging profiles [22].

The remainder of this paper is organized as follows. Section 2 introduces the proposed method, including signal preprocessing, model architecture, and evaluation metrics. Section 3 describes the datasets and presents data analysis. Section 4 covers the experimental setup, model evaluations, and additional validation with transfer learning. Finally, Section 5 concludes the paper and outlines future work.

2. Proposed Method

The proposed method predicts RUL of lithium-ion batteries, defined as the number of charge-discharge cycles remaining from the current cycle i until the battery reaches its EOL. The approach comprises two main stages: (1) a signal preprocessing pipeline for extracting informative features, and (2) a prediction model based on a hybrid deep learning architecture for estimating RUL. The overall architecture is illustrated in Figure 1. The details of these two components are presented in the following subsections.

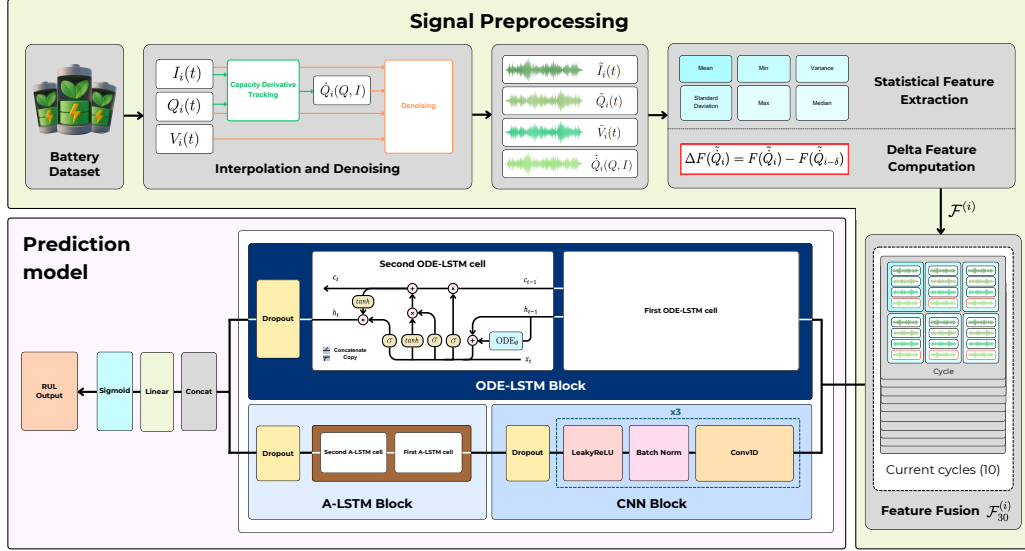


Figure 1: Overall architecture of our proposed end-to-end framework.

2.1. Signal Preprocessing

We propose a signal preprocessing pipeline that efficiently constructs a feature tensor $\mathcal{F}_{30}^{(i)}$ for each input sample, representing a sequence of 10 consecutive charge-discharge cycles. The objective of the pipeline is to reduce noise and enhance the salient characteristics of the signals. The proposed preprocessing pipeline consists of the following steps:

1. **Capacity Interpolation and Denoising:** For each charge-discharge cycle i , we first generate evenly spaced values between the minimum and maximum of the current signal $I_i(t)$. A one-dimensional interpolation method [27] is then applied, using the sorted current values as the x -coordinates and the corresponding discharge capacities as the y -coordinates. This yields the derived capacity feature $\dot{Q}_i(Q, I)$, a technique we refer to as *Capacity Derivative Tracking*. Consequently, we obtain the data sequences $I_i(t)$, $V_i(t)$, $Q_i(t)$, and $\dot{Q}_i(Q, I)$. Each of these sequences is subsequently denoised using a selected filtering method—specifically, the Savitzky–Golay filter [33]—resulting in the smoothed signals $\tilde{x}_i \in \{\tilde{I}_i(t), \tilde{V}_i(t), \tilde{Q}_i(t), \tilde{Q}_i(Q, I)\}$.
2. **Statistical Feature Extraction:** From each denoised sequence \tilde{x}_i ,

we compute a feature vector F consisting of six statistical descriptors:

$$F(\tilde{x}_i) = [\mu(\tilde{x}_i), \sigma(\tilde{x}_i), \min(\tilde{x}_i), \max(\tilde{x}_i), \text{Var}(\tilde{x}_i), \text{Median}(\tilde{x}_i)], \quad (1)$$

where μ is the mean, σ is the standard deviation, \min and \max denote the minimum and maximum values, Var is the variance, and Median is the median of the smoothed signal \tilde{x}_i .

3. **Delta Feature Computation:** To capture temporal dynamics, we compute the change in derived features $F(\tilde{Q}_i)$ over a cycle interval δ (set to 9 charge-discharge cycles, based on the optimal configuration identified in Figure 4):

$$\Delta F(\tilde{Q}_i) = F(\tilde{Q}_i) - F(\tilde{Q}_{i-\delta}), \quad (2)$$

where $\Delta F(\tilde{Q}_i)$ represents the change in derived features between cycle i and the previous cycle $i - \delta$.

4. **Feature Fusion:** For each charge-discharge cycle i where $i > \delta$, we extract the following feature vectors: $F(\tilde{I}_i)$, $F(\tilde{V}_i)$, $F(\tilde{Q}_i)$, $\Delta F(\tilde{Q}_i)$, each of size \mathbb{R}^6 . Together, they form a fused feature matrix of size $\mathbb{R}^{4 \times 6}$:

$$\mathcal{F}^{(i)} = [F(\tilde{I}_i), F(\tilde{V}_i), F(\tilde{Q}_i), \Delta F(\tilde{Q}_i)] \in \mathbb{R}^{4 \times 6}. \quad (3)$$

For RUL prediction, each input sample comprises data from 10 uniformly spaced cycles selected within a 30-cycle window (i.e., one cycle every three cycles), following the strategy in [22]. The resulting input sample is:

$$\mathcal{F}_{30}^{(i)} \in \mathbb{R}^{10 \times 4 \times 6}. \quad (4)$$

2.2. Prediction Model

Each input sample $\mathcal{F}_{30}^{(i)}$, as described in the previous section, is fed into the proposed prediction model to estimate the RUL. Our prediction model comprises three primary components: CNN block, A-LSTM block, and LSTM-ODE block. Among these, A-LSTM block is adopted from the prior work [16], while the other components are tailored.

In CNN block. The input tensor $\mathcal{F}_{30}^{(i)}$ is first reshaped into a sequence of 10 time steps, each represented by a 24-dimensional feature vector. This sequence is then passed through a stack of three one-dimensional convolutional layers with a shared kernel size of 5 and progressively increasing channel dimensions— H , $2H$, and $4H$, where $H = 64$ —consistent with the optimal configuration identified in Figure 5. Each convolution operation is followed by batch normalization [4], a Leaky ReLU activation [47], and dropout [42] for regularization. A fixed dropout rate of 0.3 is applied across all dropout layers in the prediction model. The resulting output is a feature map of shape $\mathbb{R}^{10 \times 256}$, effectively capturing temporal dependencies and patterns within the cycle window.

A-LSTM Block. The feature map from the CNN block is fed into a two A-LSTM cells [16] with a sequence length of 10. The input size to the A-LSTM is 256, and the hidden size is 128. This block captures long-range temporal dependencies with attention mechanisms across the sequence. The hidden state at the final timestep is extracted and regularized via dropout, resulting in an output vector of shape \mathbb{R}^{128} .

ODE-LSTM Block. This block processes the input sample $\mathcal{F}_{30}^{(i)}$ by reshaping it into a matrix of shape $\mathbb{R}^{10 \times 24}$, while preserving the temporal order. A continuous time sequence $t \in [0, 1]$ with 10 uniformly spaced points is generated to simulate continuous-time dynamics. Both the reshaped input and time sequence are fed into two stacked ODE-LSTM cells, with each input size 24 and hidden size 256. The final hidden state is extracted and passed through a dropout layer, resulting in an output vector of size \mathbb{R}^{256} .

Our ODE-LSTM network extends the traditional long short-term memory (LSTM) [36] architecture by integrating a neural ordinary differential equation (ODE) to model the continuous evolution of hidden states between discrete inputs. The computation proceeds in two stages: (1) continuous-time evolution of the hidden state using an ODE solver, and (2) discrete-time update using the LSTM cell, as follows:

$$\begin{aligned}
\tilde{h}_t &= h_{t-1} + \text{ODE}_\theta(h_{t-1}, t-1, t), \\
i_t &= \sigma(W_i[x_t; \tilde{h}_t]), \\
f_t &= \sigma(W_f[x_t; \tilde{h}_t]), \\
o_t &= \sigma(W_o[x_t; \tilde{h}_t]), \\
\tilde{c}_t &= \tanh(W_c[x_t; \tilde{h}_t]), \\
c_t &= f_t \odot c_{t-1} + i_t \odot \tilde{c}_t, \\
h_t &= o_t \odot \tanh(c_t),
\end{aligned}$$

where ODE_θ models the continuous transition of hidden states and is implemented using Euler integration:

$$\text{ODE}_\theta(h, t_0, t_1) = \int_{t_0}^{t_1} f_\theta(h(t), t) dt.$$

Here, f_θ is a neural network (implemented as a linear layer), and $[\cdot; \cdot]$ denotes vector concatenation. x_t is the input vector at time step t . h_t is the hidden state at time t . \tilde{h}_t is the hidden state after ODE evolution from t_{t-1} to t_t . c_t is the cell state at time t . $\sigma(\cdot)$ denotes the sigmoid activation function, and $\tanh(\cdot)$ denotes the hyperbolic tangent activation. W_i , W_f , W_o , and W_c are trainable weight matrices for the input, forget, output, and candidate gates, respectively. \odot denotes element-wise multiplication.

The output features from the CNN + A-LSTM and ODE-LSTM branches are concatenated into a single vector of dimension 384 and passed through a fully connected layer followed by a sigmoid activation to predict the RUL. Our proposed hybrid deep learning model is trained using Mean Squared Error (MSE) loss function, optimized with the AdamW optimizer [19]. The MSE loss is defined as:

$$\mathcal{L}_{\text{MSE}} = \frac{1}{N} \sum_{i=1}^N (y_i - \hat{y}_i)^2.$$

Where N is the number of training samples, y_i denotes the ground truth RUL of the i -th cycling sample, and \hat{y}_i denotes the predicted RUL of the i -th sample.

2.3. Evaluation Metrics

To assess the performance of RUL prediction, we employ three evaluation metrics: Root Mean Square Error ($RMSE$) [43], R-squared (R^2) [41], and Mean Absolute Percentage Error ($MAPE$) [6]. These metrics are defined as follows:

$$RMSE(y_i, \hat{y}_i) = \sqrt{\frac{1}{n} \sum_{i=1}^n (y_i - \hat{y}_i)^2},$$
$$MAPE(y_i, \hat{y}_i) = \frac{1}{n} \sum_{i=1}^n \frac{|y_i - \hat{y}_i|}{y} \times 100,$$
$$R^2(y, \hat{y}) = 1 - \frac{\sum_{i=1}^n (y_i - \hat{y}_i)^2}{\sum_{i=1}^n (y_i - \bar{y})^2}.$$

Here, y_i represents the observed RUL, and \hat{y}_i represents the predicted RUL. Additionally, y refers to the cycle life. The performance improves with lower values of $RMSE$ and $MAPE$, and a higher value of R^2 .

3. Dataset

3.1. Dataset Description

3.1.1. First dataset

The dataset [34] features a comprehensive study of 124 lithium-ion batteries (LIBs) with LFP/graphite chemistry, focusing on various fast-charging conditions while maintaining consistent discharging parameters. Each battery in the dataset has a nominal capacity of 1.1 Ah and a nominal voltage of 3.3 V, with cycle lifespans ranging from 150 to 2,300 cycles, highlighting a broad range of battery longevity. All LIBs underwent uniform discharge procedures, involving a constant current discharge at a rate of 4 C until the voltage reached 2 V, followed by a constant voltage discharge at 2 V until the current dropped to C/50. Charging was conducted at rates between 3.6 C and 6 C under controlled temperature conditions of 30°C in an environmental chamber. The dataset comprises roughly 96,700 cycles, making it one of the largest datasets exploring various fast-charging protocols. It is divided into three sections: a training set with 41 LIBs, a validation set with 43 LIBs, and a test set with 40 LIBs.

3.1.2. Second dataset

The dataset [22], which involved varying discharge conditions while maintaining consistent fast-charging conditions, was collected from a battery degradation experiment. This experiment utilized 77 cells (LFP/graphite A123 APR18650M1A), each with a nominal capacity of 1.1 Ah and a nominal voltage of 3.3 V. Each cell underwent a distinct multi-stage discharge protocol, while all cells shared the same fast-charging protocol. The experiment was carried out in two thermostatic chambers, with a controlled temperature of 30°C. The dataset contains a total of 146,122 discharge cycles, making it one of the largest datasets that incorporate various discharge protocols. The cycle life of the cells ranges from 1,100 to 2,700 cycles, with an average of 1,898 cycles and a standard deviation of 387 cycles. The discharge capacity as a function of cycle number shows a broad distribution of cycle lives. The dataset is divided into two parts: In 55 LIBs predefined for training, 90% is used for the training set, 10% for the validation set, and the remaining 22 LIBs are used as the test set.

3.2. Data Analysis

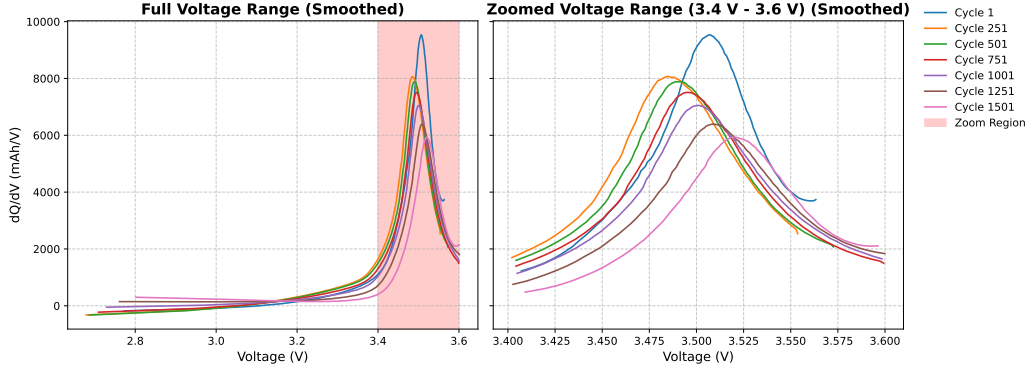


Figure 2: Smoothed incremental capacity (dQ/dV) curves during charging for selected cycles on a battery cell from the second dataset: full voltage range (left) and zoomed-in region (3.4–3.6 V, right).

The degradation of LIBs through charge-discharge cycles is primarily caused by the LLI, leading to irreversible capacity fade. IC analysis, which plots dQ/dV versus voltage, is a widely used diagnostic tool for identifying LLI-related degradation [1].

As shown in Figure 2, smoothed IC curves during constant current charging illustrate degradation trends in lithium-ion batteries. The position, intensity, and shape of dQ/dV peaks provide key insights into electrochemical aging. Notably, the graphite peak associated with the $\text{LiC}_6 \rightarrow \text{LiC}_{12}$ phase transition [17] shifts left by over 10mV between Cycle 1 and Cycle 1501 (right plot), indicating lithium loss due to solid electrolyte interphase (SEI) formation. This irreversible process consumes lithium ions. Concurrently, the peak height drops by about 35%, signaling a decline in active lithium available for intercalation [29, 46].

Overall, LLI accounts for approximately 70% of the total observed capacity fade, based on the analysis of smoothed IC curves in Figure 2 using the methodology from [29]. Additionally, the figure reveals a capacity reduction of around 20% after 1500 cycles, with the degradation rate varying across the charge-discharge lifespan. These findings highlight the need for a robust RUL prediction method capable of capturing non-uniform aging patterns to reliably predict the RUL of lithium-ion batteries.

4. Experiments and Discussion

4.1. Experimental Setup

Our proposed RUL model is developed using the PyTorch framework. All experiments are performed on an NVIDIA 4090 GPU with 24GB of memory. Each experiment is trained for 10 epochs with a batch size of 128 and a constant learning rate of 0.0005. To minimize variability in the training process, each experiment is repeated 10 times, and the final prediction is calculated as the average of these multiple runs.

4.2. Evaluation of Signal Preprocessing

In the denoising step, to mitigate noise in voltage, current and capacity signals, four denoising techniques including Gaussian smoothing [44], Savitzky-Golay filtering [13], wavelet decomposition [8], and Kalman filtering—along with a no-denoising baseline (raw data), were evaluated on the second dataset. As shown in Figure 3, the Savitzky-Golay filter [32] achieved the optimal performance, yielding an RMSE of 169.93 (cycles). Compared to Gaussian smoothing and wavelet decomposition, the Savitzky-Golay method demonstrates superior capability in peak preservation and adaptive smoothing.

One key factor influencing the effectiveness of the Savitzky-Golay filter is the window length, which balances noise reduction and signal distortion. To determine the optimal configuration, various window lengths were tested. As shown in the right panel of Figure 3, a window length of 191 points provides the best trade-off between denoising and feature preservation. Consequently, the Savitzky-Golay filter with a window length of 191 is adopted in the denoising stage of our signal preprocessing pipeline.

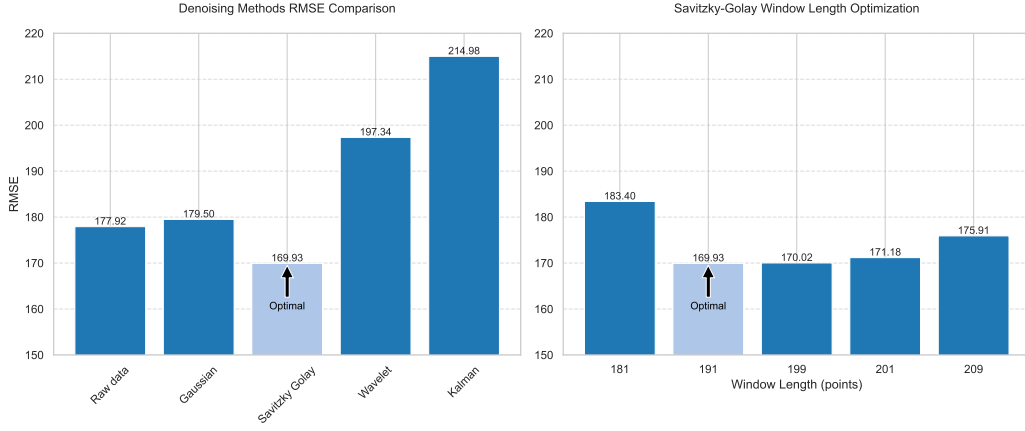


Figure 3: RMSE comparison of different denoising methods (left) and the impact of the window length parameter on Savitzky-Golay method (right).

Figure 4 on the left shows that using only derived features results in the highest RMSE of 252.52, indicating that relying solely on derived features leads to poor predictive performance. In contrast, the feature combination of I, V, Q, and dQ(I) achieves the lowest RMSE value of 162.37, outperforming other feature sets. The strong contribution of dQ(I) highlights the effectiveness of the proposed Capacity Derivative Tracking method in estimating discharge data. By aligning discharge capacity values with corresponding current measurements, this method provides a more consistent representation of the current–discharge capacity relationship over time, enhancing the prediction performance of the model.

After the interpolation step, the difference in extracted features between each cycle and the one occurring *delta* steps earlier is computed. The choice of the *delta* parameter is important, as it determines the temporal resolution of feature variation. To assess its impact, we evaluated *delta* values ranging from 1 to 10, as shown in Figure 4 on the right. Among these, a *delta* value

of 9 achieved the best performance, yielding the lowest RMSE of 162.37.

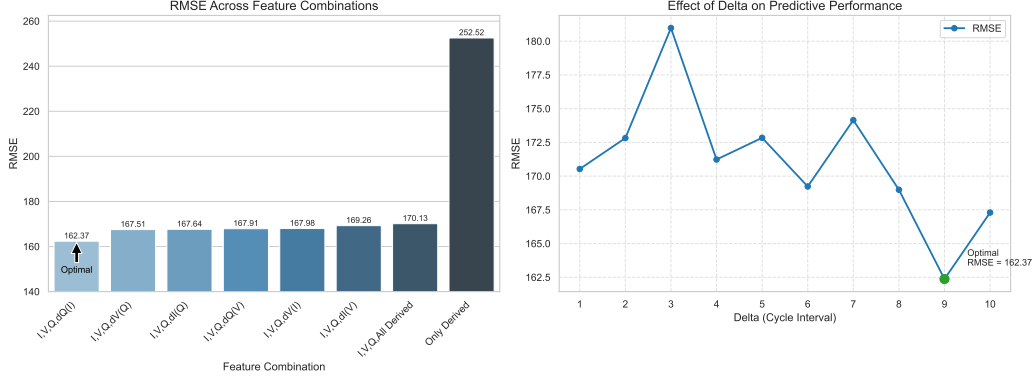


Figure 4: RMSE comparison of feature combinations (left) with δ set to 9, and the effect of δ on predictive performance (right).

4.3. Validation of Prediction Model

As shown in Table 1, the proposed signal preprocessing pipeline, which includes the derived capacity feature $\dot{Q}_i(Q, I)$, consistently improves the performance of all evaluated models. Notably, our proposed prediction model, CNN + A-LSTM + ODE-LSTM, achieves the best results, with the lowest RMSE of 158.09, highest R^2 score of 0.89, and lowest MAPE of 6.95%. These results confirm the effectiveness of combining CNN with A-LSTM and ODE-LSTM components, especially when enriched with the derived capacity feature.

Table 1: Performance comparison of deep learning models on the testing data of the second dataset.

| Our Signal Preprocessing | Model | RMSE ↓ | R^2 ↑ | MAPE (%) ↓ |
|--------------------------|--------------------------------|---------------|-------------|-------------|
| W/o $\dot{Q}_i(Q, I)$ | Attentional LSTM (A-LSTM) | 174.83 | 0.84 | 8.14 |
| | CNN + A-LSTM | 167.37 | 0.85 | 7.62 |
| | CNN + A-LSTM + ODE-A-LSTM | 168.51 | 0.84 | 8.01 |
| | CNN + A-LSTM + ODE-LSTM (Ours) | 163.31 | 0.85 | 7.54 |
| With $\dot{Q}_i(Q, I)$ | Attentional LSTM (A-LSTM) | 168.09 | 0.87 | 7.47 |
| | CNN + A-LSTM | 169.02 | 0.87 | 7.40 |
| | CNN + A-LSTM + ODE-A-LSTM | 170.69 | 0.87 | 8.03 |
| | CNN + A-LSTM + ODE-LSTM (Ours) | 158.09 | 0.89 | 6.95 |

To assess the impact of various configurations on the prediction model performance, we conducted a series of experiments evaluating RMSE across

different settings. These included activation functions (GeLU [14], HardSwish [2], ReLU [3], LeakyReLU), ODE integration schemes (RK4 [39], Midpoint [48], Heun2/3 [30], Euler [31]), convolutional kernel sizes, hidden layer sizes, and the selection of the relative time variable R_t (RT), as defined in the A-LSTM paper [16]. Each configuration was isolated while keeping other components fixed to ensure fair comparison. The results, visualized in Figure 5, indicate that specific choices—such as using LeakyReLU as the activation function, Euler for ODE integration, a kernel size of $k = 5$, a hidden size of 64, and first RT in A-LSTM block yielded lower RMSE values. These optimal settings were highlighted in the figure to emphasize their contribution to improved predictive accuracy. This analysis validates the importance of fine-tuning model configurations to achieve optimal performance in the target task.

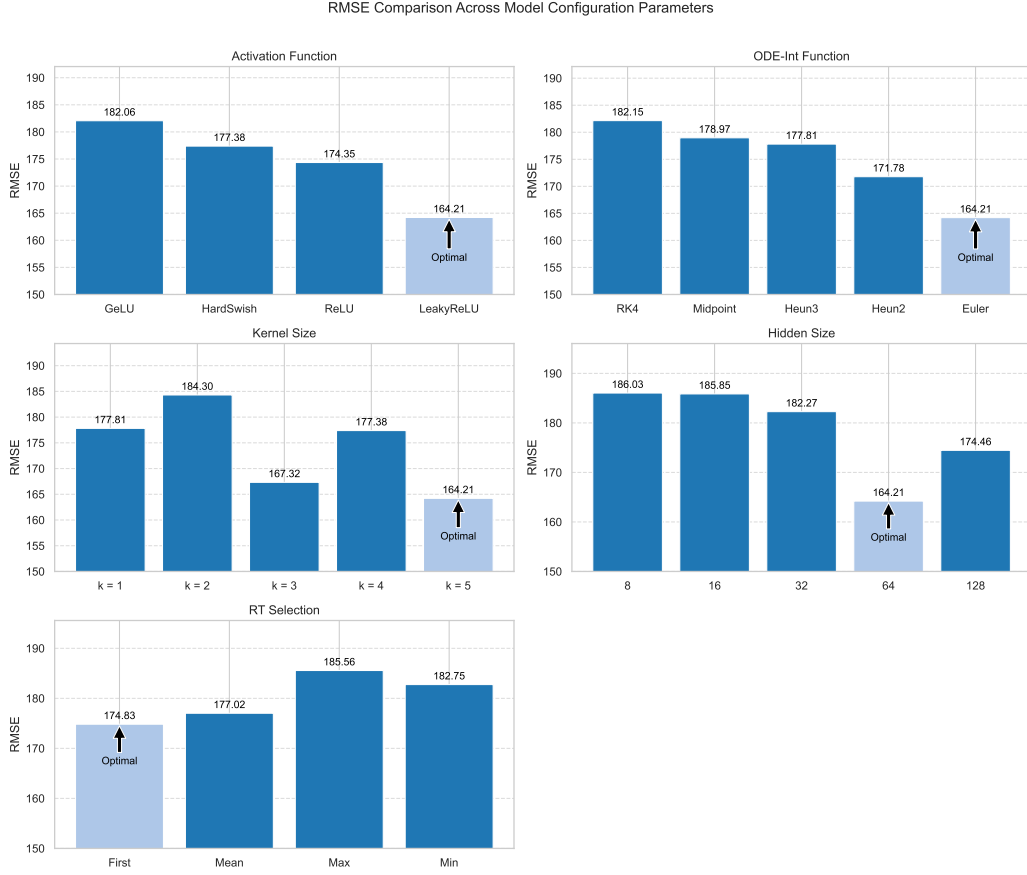


Figure 5: RMSE Comparison Across Configurations of the Proposed Prediction Model.

Figure 6 illustrates the RUL prediction performance of the proposed model across eight test battery cells taken from the test sets of two battery datasets. The red curves represent the predicted RUL, while the black curves denote the ground truth. Across all battery cells, the predicted RUL closely follows the actual degradation trend, confirming the model’s ability to generalize across diverse data distributions. Notably, the model successfully captures the nonlinear degradation behavior, particularly in cells such as b1c31 and 10-4, where the actual RUL exhibits mild fluctuations. Although slight overestimations appear in the early cycles and near EOL periods, the predictions remain consistently aligned with observed values.

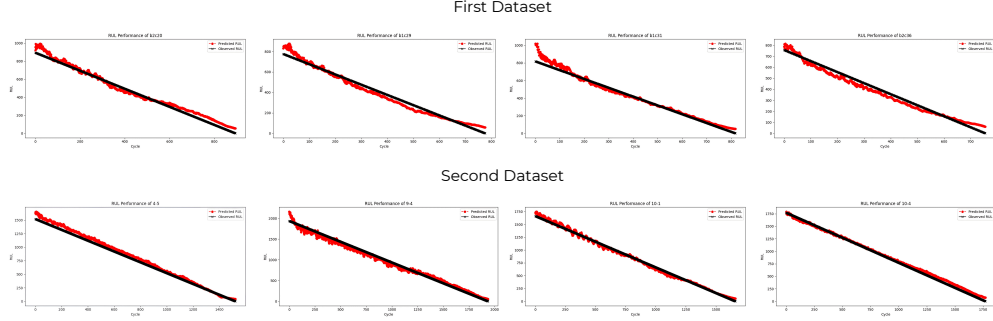


Figure 6: Comparison of predicted RUL and actual RUL for some batteries from the first and the second datasets.

Table 2 presents a performance comparison between the proposed model and several baseline methods, including traditional machine learning models and the deep learning-based approach proposed in [22], across two battery datasets. On the first dataset, the proposed model significantly outperforms both ElasticNet [10] and XGBoostRegression [40], achieving the lowest RMSE of 101.59, the highest R^2 score of 0.82, and a substantially reduced MAPE of 8.29%. Similarly, on the second dataset, the proposed model surpasses all other methods, including the baseline model from [22], with an RMSE of 158.09, an R^2 score of 0.89, and the lowest MAPE of 6.95%. These results highlight the effectiveness and generalizability of the proposed approach across different data distributions.

Table 2: Comparison of the proposed approach with machine learning and existing approaches on both the first and second datasets.

| Dataset | Method | RMSE ↓ | R^2 ↑ | MAPE (%) ↓ |
|----------------|-------------------|---------------|-------------|-------------|
| First dataset | ElasticNet | 319.98 | -0.20 | 26.70 |
| | XGBoostRegression | 156.33 | 0.70 | 12.19 |
| | Our model | 101.59 | 0.82 | 8.29 |
| Second dataset | ElasticNet | 575.54 | -0.20 | 26.67 |
| | XGBoostRegression | 169.88 | 0.87 | 7.37 |
| | [22] | 186 | 0.804 | 8.72 |
| | Our model | 158.09 | 0.89 | 6.95 |

4.4. Extended Validation of Transfer Learning on the Prediction Model

To evaluate the generalization capability of the proposed model across different battery datasets, we conducted a series of transfer learning experiments as detailed in Table 3. In cases involving upper and lower half splits, the training data were divided into two groups of battery cells based on cycle life: cells with a cycle life below the median of the cycle lives of the training set were assigned to the lower half, while those above the median were placed in the upper half. These experiments explore various scenarios in which the model is pre-trained on one dataset and fine-tuned on another, simulating real-world applications where labeled data in the target domain is scarce.

Table 3: Configuration of transfer learning strategies for each case, showing the datasets used for pre-training and fine-tuning with their respective testing sets.

| Testing data of | Case | Pre-Training | Fine-tuning |
|-----------------|------|--|---|
| First dataset | 1 | Entire training data of the first dataset | – |
| | 2 | Entire training data of the second dataset | – |
| | 3.1 | Entire training data of the second dataset | Upper half of training data from the first dataset |
| | 3.2 | Entire training data of the second dataset | Lower half of training data from the first dataset |
| | 4 | Entire training data of the second dataset | Entire training data of the first dataset |
| Second dataset | 5 | Entire training data of the second dataset | – |
| | 6 | Entire training data of the first dataset | – |
| | 7.1 | Entire training data of the first dataset | Upper half of training data from the second dataset |
| | 7.2 | Entire training data of the first dataset | Lower half of training data from the second dataset |
| | 8 | Entire training data of the first dataset | Entire training data of the second dataset |

First, we use Case 8 to investigate the impact of different block-freezing strategies during transfer learning, shown in Table 4. Notably, freezing only the A-LSTM block yields the best overall performance, suggesting that this component captures more transferable temporal features. In contrast, freezing all three blocks (CNN, A-LSTM, and ODE-LSTM) results in severe performance degradation, underscoring the importance of model flexibility during fine-tuning. Based on these findings, we adopt this block-freezing strategy of freezing only A-LSTM block for the next experiment, as shown in Table 5.

Table 4: Performance comparison under various block-freezing strategies applied during transfer learning in Case 8 (see Table 3).

| Transfer Learning Strategy | RMSE ↓ | R^2 ↑ | MAPE (%) ↓ |
|-----------------------------|---------------|-------------|-------------|
| Freezing CNN block (1) | 166.18 | 0.88 | 7.21 |
| Freezing A-LSTM block (2) | 157.92 | 0.88 | 6.88 |
| Freezing ODE-LSTM block (3) | 159.64 | 0.87 | 6.79 |
| (1) + (2) | 170.05 | 0.86 | 7.48 |
| (1) + (3) | 179.4 | 0.85 | 8.04 |
| (2) + (3) | 161.98 | 0.86 | 7.01 |
| (1) + (2) + (3) | 282.69 | 0.69 | 12.79 |

The results, summarized in Table 5, demonstrate that direct transfer (Cases 2 and 6) without fine-tuning leads to poor performance, with high RMSE and negative R^2 , indicating a significant mismatch in data distributions between the two datasets. However, introducing fine-tuning with partial data from the target domain (Cases 3.1, 3.2, 7.1, and 7.2) noticeably improves model accuracy, with Case 7.2 achieving a strong balance (RMSE = 201.63, R^2 = 0.81, MAPE = 8.63%). Full fine-tuning on the target domain after pre-training (Cases 4 and 8) yields performance close to or even better than training directly on the target dataset (Cases 1 and 5), with Case 8 achieving the best results on the second dataset (RMSE = 157.92, R^2 = 0.88, MAPE = 6.88%).

Table 5: Performance comparison of our proposed model on different training strategies with Transfer Learning on both first and second dataset.

| Case | RMSE ↓ | R^2 ↑ | MAPE (%) ↓ |
|------|---------------|-------------|-------------|
| 1 | 101.59 | 0.82 | 8.29 |
| 2 | 543.56 | -2.58 | 46.66 |
| 3.1 | 160.98 | 0.61 | 14.4 |
| 3.2 | 290.75 | 0.00 | 23.31 |
| 4 | 123.44 | 0.76 | 10.64 |
| 5 | 158.09 | 0.89 | 6.95 |
| 6 | 800.23 | -1.21 | 35.76 |
| 7.1 | 231.12 | 0.73 | 11.69 |
| 7.2 | 201.63 | 0.81 | 8.63 |
| 8 | 157.92 | 0.88 | 6.88 |

5. Conclusion

This study presents an robust approach for predicting the RUL of lithium-ion batteries by integrating an advanced signal processing pipeline with a deep learning prediction model. The signal preprocessing pipeline, comprising Capacity Interpolation and Denoising, Statistical Feature Extraction, Delta Feature Computation, and Feature Fusion, effectively captures the degradation dynamics over charge-discharge cycles. The proposed prediction model, combining CNN, A-LSTM, and ODE-LSTM blocks, demonstrates strong capabilities in modeling both discrete and continuous time behaviors of battery aging. Notably, the integration of our proposed CNN and ODE-LSTM block enhances the prediction model’s ability. The model is further evaluated using transfer learning across different learning strategies and source data partitioning scenarios. Results indicate that the model maintains robust performance even when trained on limited data, underscoring its adaptability and effectiveness in data-constrained environments. Experimental validation on two large-scale datasets confirms that our method significantly outperforms a baseline deep learning approach and traditional machine learning techniques. These results highlight the potential of the proposed approach for practical deployment in predictive maintenance systems, contributing to improved reliability and longevity of battery-powered applications. Future work will explore the generalizability of the method across

different battery chemistries and usage scenarios. Additionally, efforts will be directed toward real-time deployment on edge devices.

Contact Information

For access to the code and further information about this proposed system, please contact AIWARE Limited Company at: <https://aiware.website/Contact>

References

- [1] David Anseán, Víctor Manuel García, Manuela González, Cecilio Blanco-Viejo, Juan Carlos Viera, Yoana Fernández Pulido, and Luciano Sánchez. Lithium-ion battery degradation indicators via incremental capacity analysis. *IEEE Transactions on Industry Applications*, 55(3):2992–3002, 2019.
- [2] R Avenash and Prashanth Viswanath. Semantic segmentation of satellite images using a modified cnn with hard-swish activation function. In *VISIGRAPP (4: VISAPP)*, pages 413–420, 2019.
- [3] Chaity Banerjee, Tathagata Mukherjee, and Eduardo Pasiliao Jr. An empirical study on generalizations of the relu activation function. In *Proceedings of the 2019 ACM Southeast Conference*, pages 164–167, 2019.
- [4] Nils Bjorck, Carla P Gomes, Bart Selman, and Kilian Q Weinberger. Understanding batch normalization. *Advances in neural information processing systems*, 31, 2018.
- [5] Yunhong Che, Jia Guo, Yusheng Zheng, Daniel-Ioan Stroe, Wenxue Liu, Xiaosong Hu, and Remus Teodorescu. Unlocking interpretable prediction of battery random discharge capacity with domain adaptative physics constraint. *Advanced Energy Materials*, page 2405506, 2025.
- [6] Arnaud De Myttenaere, Boris Golden, Bénédicte Le Grand, and Fabrice Rossi. Mean absolute percentage error for regression models. *Neurocomputing*, 192:38–48, 2016.

- [7] Xinghao Du, Jinhao Meng, Yassine Amirat, Fei Gao, and Mohamed Benbouzid. Feature selection strategy optimization for lithium-ion battery state of health estimation under impedance uncertainties. *Journal of Energy Chemistry*, 101:87–98, 2025.
- [8] Burhan Ergen. *Signal and image denoising using wavelet transform*. InTech London, UK, 2012.
- [9] Kangping Gao, Ziyi Huang, Chunting Lyu, and Chengqi Liu. Multi-scale prediction of remaining useful life of lithium-ion batteries based on variational mode decomposition and integrated machine learning. *Journal of Energy Storage*, 99:113372, 2024.
- [10] Chris Hans. Elastic net regression modeling with the orthant normal prior. *Journal of the American Statistical Association*, 106(496):1383–1393, 2011.
- [11] Shanling Ji, Jianxiong Zhu, Zhiyang Lyu, Heze You, Yifan Zhou, Liudong Gu, Jinqing Qu, Zhijie Xia, Zhisheng Zhang, and Haifeng Dai. Deep learning enhanced lithium-ion battery nonlinear fading prognosis. *Journal of Energy Chemistry*, 78:565–573, 2023.
- [12] Zhipeng Jiao, Hongda Wang, Jianchun Xing, Qiliang Yang, Man Yang, Yutao Zhou, and Jiubin Zhao. Lightgbm-based framework for lithium-ion battery remaining useful life prediction under driving conditions. *IEEE Transactions on Industrial Informatics*, 19(11):11353–11362, 2023.
- [13] Malek Karaim, Aboelmagd Noureldin, and Tashfeen B Karamat. Low-cost imu data denoising using savitzky-golay filters. In *2019 International Conference on Communications, Signal Processing, and their Applications (ICCSPA)*, pages 1–5. IEEE, 2019.
- [14] Minhyeok Lee. Mathematical analysis and performance evaluation of the gelu activation function in deep learning. *Journal of Mathematics*, 2023(1):4229924, 2023.
- [15] Xingjun Li, Dan Yu, Vilsen Søren Byg, and Store Daniel Ioan. The development of machine learning-based remaining useful life prediction for lithium-ion batteries. *Journal of Energy Chemistry*, 82:103–121, 2023.

- [16] Fan Liu, Xingshe Zhou, Jinli Cao, Zhu Wang, Tianben Wang, Hua Wang, and Yanchun Zhang. Anomaly detection in quasi-periodic time series based on automatic data segmentation and attentional lstm-cnn. *IEEE Transactions on Knowledge and Data Engineering*, 34(6):2626–2640, 2020.
- [17] Qiang Liu, Shuai Li, Senhao Wang, Xianggong Zhang, Sisi Zhou, Ying Bai, Jieyun Zheng, and Xia Lu. Kinetically determined phase transition from stage ii (lic12) to stage i (lic6) in a graphite anode for li-ion batteries. *The Journal of Physical Chemistry Letters*, 9(18):5567–5573, 2018. PMID: 30198723.
- [18] Yunpeng Liu, Bo Hou, Moin Ahmed, Zhiyu Mao, Jiangtao Feng, and Zhongwei Chen. A hybrid deep learning approach for remaining useful life prediction of lithium-ion batteries based on discharging fragments. *Applied Energy*, 358:122555, 2024.
- [19] Ilya Loshchilov and Frank Hutter. Decoupled weight decay regularization. *arXiv preprint arXiv:1711.05101*, 2017.
- [20] Guijun Ma, Zidong Wang, Weibo Liu, Jingzhong Fang, Yong Zhang, Han Ding, and Ye Yuan. Estimating the state of health for lithium-ion batteries: A particle swarm optimization-assisted deep domain adaptation approach. *IEEE/CAA Journal of Automatica Sinica*, 10(7):1530–1543, 2023.
- [21] Guijun Ma, Zidong Wang, Weibo Liu, Jingzhong Fang, Yong Zhang, Han Ding, and Ye Yuan. A two-stage integrated method for early prediction of remaining useful life of lithium-ion batteries. *Knowledge-Based Systems*, 259:110012, 2023.
- [22] Guijun Ma, Songpei Xu, Benben Jiang, Cheng Cheng, Xin Yang, Yue Shen, Tao Yang, Yunhui Huang, Han Ding, and Ye Yuan. Real-time personalized health status prediction of lithium-ion batteries using deep transfer learning. *Energy & Environmental Science*, 15(10):4083–4094, 2022.
- [23] Guijun Ma, Yong Zhang, Cheng Cheng, Beitong Zhou, Pengchao Hu, and Ye Yuan. Remaining useful life prediction of lithium-ion batteries

- based on false nearest neighbors and a hybrid neural network. *Applied Energy*, 253:113626, 2019.
- [24] Liang Ma, Jinpeng Tian, Tieling Zhang, Qinghua Guo, and Chi Yung Chung. Enhanced battery life prediction with reduced data demand via semi-supervised representation learning. *Journal of Energy Chemistry*, 101:524–534, 2025.
 - [25] Liang Ma, Jinpeng Tian, Tieling Zhang, Qinghua Guo, and Chunsheng Hu. Accurate and efficient remaining useful life prediction of batteries enabled by physics-informed machine learning. *Journal of Energy Chemistry*, 91:512–521, 2024.
 - [26] Huixing Meng and Yan-Fu Li. A review on prognostics and health management (phm) methods of lithium-ion batteries. *Renewable and Sustainable Energy Reviews*, 116:109405, 2019.
 - [27] NumPy Developers. `numpy.interp` — NumPy v2.1 Manual. <https://numpy.org/doc/2.1/reference/generated/numpy.interp.html>, 2024. Accessed: 2025-05-15.
 - [28] Simin Peng, Yifan Miao, Rui Xiong, Jiawei Bai, Mengzeng Cheng, and Michael Pecht. State of charge estimation for a parallel battery pack jointly by fuzzy-pi model regulator and adaptive unscented kalman filter. *Applied energy*, 360:122807, 2024.
 - [29] Matthew B. Pinson and Martin Z. Bazant. Theory of sei formation in rechargeable batteries: Capacity fade, accelerated aging and lifetime prediction. *Journal of The Electrochemical Society*, 160(2):A243, dec 2012.
 - [30] Nidhal Q Saadoon, Noora T Abduirazzaq, Adel S Hussain, Noora A Mohammed, Emad A Az-Zo’bi, and Mohammad A Tashtoush. Numerical solutions for fuzzy stochastic ordinary differential equations using heun’s method with a dual-wiener process framework. *Mathematical Modelling of Engineering Problems*, 12(3), 2025.
 - [31] ZULZAMRI Salleh. Ordinary differential equations (ode) using euler’s technique and scilab programming. *Mathematical Models and Methods in Modern Science*, 20(4):264–269, 2012.

- [32] Omid Sayadi and Mohammad Bagher Shamsollahi. Ecg denoising and compression using a modified extended kalman filter structure. *IEEE transactions on biomedical engineering*, 55(9):2240–2248, 2008.
- [33] Ronald W Schafer. What is a savitzky-golay filter?[lecture notes]. *IEEE Signal processing magazine*, 28(4):111–117, 2011.
- [34] Kristen A Severson, Peter M Attia, Norman Jin, Nicholas Perkins, Benben Jiang, Zi Yang, Michael H Chen, Muratahan Aykol, Patrick K Herring, Dimitrios Fraggedakis, et al. Data-driven prediction of battery cycle life before capacity degradation. *Nature Energy*, 4(5):383–391, 2019.
- [35] Syed Abbas Ali Shah, Sajawal Gul Niazi, Shangqi Deng, Hafiz Muhammad Hamza Azam, Khalil Mian Muhammad Yasir, Jay Kumar, Ziqiang Xu, and Mengqiang Wu. A novel positional encoded attention-based long short-term memory network for state of charge estimation of lithium-ion battery. *Journal of Power Sources*, 590:233788, 2024.
- [36] Alex Sherstinsky. Fundamentals of recurrent neural network (rnn) and long short-term memory (lstm) network. *Physica D: Nonlinear Phenomena*, 404:132306, 2020.
- [37] Gina Sierra, Marcos Orchard, Kai Goebel, and Chetan Kulkarni. Battery health management for small-size rotary-wing electric unmanned aerial vehicles: An efficient approach for constrained computing platforms. *Reliability Engineering & System Safety*, 182:166–178, 2019.
- [38] Jinghua Sun and Josef Kainz. State of health estimation for lithium-ion batteries based on current interrupt method and genetic algorithm optimized back propagation neural network. *Journal of Power Sources*, 591:233842, 2024.
- [39] Kim Gaik Tay, Sie Long Kek, and Rosmila Abdul-Kahar. A spreadsheet solution of a system of ordinary differential equations using the fourth-order runge-kutta method. *Spreadsheets in education (eJSiE)*, 5(2):1–10, 2012.
- [40] Ruoran Wang, Luping Wang, Jing Zhang, Min He, and Jianguo Xu. Xgboost machine learning algorism performed better than regression

models in predicting mortality of moderate-to-severe traumatic brain injury. *World Neurosurgery*, 163:e617–e622, 2022.

- [41] Shuai Wang, Hongyan Ma, Yingda Zhang, Shengyan Li, and Wei He. Remaining useful life prediction method of lithium-ion batteries is based on variational modal decomposition and deep learning integrated approach. *Energy*, 282:128984, 2023.
- [42] Colin Wei, Sham Kakade, and Tengyu Ma. The implicit and explicit regularization effects of dropout. In *International conference on machine learning*, pages 10181–10192. PMLR, 2020.
- [43] Cort J Willmott and Kenji Matsuura. Advantages of the mean absolute error (mae) over the root mean square error (rmse) in assessing average model performance. *Climate research*, 30(1):79–82, 2005.
- [44] Alle Meije Wink and Jos BTM Roerdink. Denoising functional mr images: a comparison of wavelet denoising and gaussian smoothing. *IEEE transactions on medical imaging*, 23(3):374–387, 2004.
- [45] Junyi Xia, Qionglin Shi, Haomiao Li, Min Zhou, Wei Wang, Kangli Wang, and Kai Jiang. Historical data-independent remaining useful life prediction method based on dual-input deep learning neural network. *Journal of Energy Storage*, 72:108427, 2023.
- [46] Bolun Xu, Alexandre Oudalov, Andreas Ulbig, Göran Andersson, and Daniel S. Kirschen. Modeling of lithium-ion battery degradation for cell life assessment. *IEEE Transactions on Smart Grid*, 9(2):1131–1140, 2018.
- [47] Jin Xu, Zishan Li, Bowen Du, Miaomiao Zhang, and Jing Liu. Relu-plex made more practical: Leaky relu. In *2020 IEEE Symposium on Computers and communications (ISCC)*, pages 1–7. IEEE, 2020.
- [48] Ying Yu et al. On the properties of numerical solutions of dynamical systems obtained using the midpoint method. *Discrete and Continuous Models and Applied Computational Science*, 27(3):242–262, 2019.
- [49] Shuzhi Zhang, Baoyu Zhai, Xu Guo, Kaike Wang, Nian Peng, and Xiongwen Zhang. Synchronous estimation of state of health and remaining useful lifetime for lithium-ion battery using the incremental capacity

and artificial neural networks. *Journal of Energy Storage*, 26:100951, 2019.